TABLE OF CONTENTS

LIST OF FIGURES

# ABSTRACT

A new technique using direct post-implant dosimetry, which does not depend explicitly on brachytherapy seed orientation or position, was explored for a prostate and a breast case. This technique, proposed by E Sajo and ML Williams (SW), uses trace amounts of positron emitters placed in the seed capsule and uses the positron emission tomography image in conjunction with a computed tomography image (PET-CT) to compute the therapeutic dose distribution in

# CHAPTER 1

# INTRODUCTION

## 1.1 Objective of the Thesis

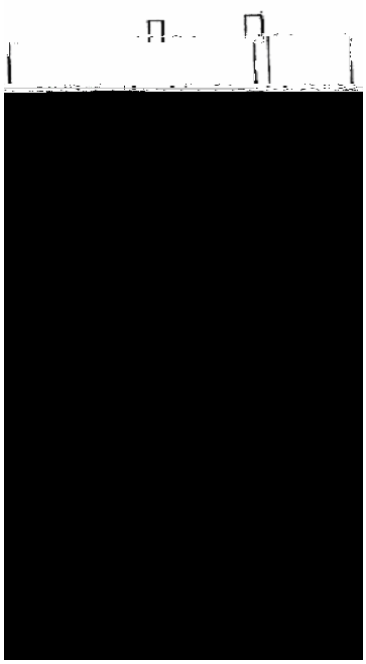

Figure 1-Geometry of a Theraseed™ Pd-103 seed.

A new technique using direct post-implant dosimetry, which does not depend explicitly on seed orientation or position, was recently proposed (Sajo and Williams, 2004). This method could eliminate some of the errors in the dose computations associated with seed localization, seed shadowing and medium heterogeneity while accelerating the process of dosimetry. This technique uses a positron emitter in tracer quantities inside the seed capsule. The dose due to the annihilation photons can be obtained by the observations using PET/CT. Subsequently, the therapeutic dose may be calculated from the annihilation dose, as described in the third section of this thesis. The activity of the positron marker isotope is a fraction of the activity of the therapeutic isotope. The radiation dose of the marker isotope delivered beyond the immediate vicinity of the seed is low because the marker isotope is adapted to have an activity of an order of magnitude lower than the activity of the therapeutic isotope. Therefore the presence of the marker isotope should not alter the therapeutic characteristics of the seed.

Dose computation based on the observed annihilation dose entails use of therapeutic and positron Green's functions to scale the positron dose in Fourier space which gives the therapeutic dose in Fourier space. The objective of this thesis is to verify that for one seed the proposed technique (Sajo and Williams, 2004) works. This entailed both experimental and computational work, as outlined here.

VI.

energy is 0.215 MeV, their range in the stainless steel seed encapsulation is shorter than the wall thickness. Therefore, all annihilations will take place inside the seed.

The PET images were subsequently analyzed and pixel-wise activities were extracted. These activities represent the detected annihilation events in the pixels. The resolution of the images, the effect of false counts, and other details will be discph1r.bie8

# CHAPTER 2

# BACKGROUND AND SIGNIFICANCE

2.1 Background 0006315 Tc0(wtate Cancer.89 ET6 T651.84 170.34 0.60 Twref2 1 12 90 38.7260.34 6530 g

placed on these images, which represents template coordinates. The template is the physical grid that is placed on the patient to guide needles to the proper position.

equivalent. Recent studies indicate that the seed shadowing effect, when correctly computed, can amount to a 3% to 5% discrepancy from the case when the individually computed doses are superimposed (Yegin and Rogers, 2004; Carrier, 2006). When the prostate tissue composition is also taken into account, the total discrepancy from water-based dose computations using the superposition technique is up to about 13% (Carrier, 2006). Additional confounding factors, such as heterogeneities in prostate composition, which is due to post-implant edema and needle traces, further increase the discrepancy between the traditionally computed doses, using for example the AAPM Task Group Report 43 method (Nath et al, 1995; Rivard et al, 2004), and the correctly computed doses using rigorous radiation transport methods (Jarrett and Sajo, 2005).

## 2.2 Background on Breast Cancer

Just as prostate cancer has the highest incidence of all cancers in males; breast cancer has the highest incidence of all cancers in women (excluding skin cancer). With better screening, the number of incidences has increased in recent years; there were over 178,000 cases in 1998. After removing a breast tumor with surgery, irradiating the tumor bed is often done. One method of irradiating the tumor bed is by using external beam 3D conformal radiation therapy. The other method, in the case of lumpectomy, is by using breast brachytherapy. A new and minimally invasive means of brachytherapy for partial breast irradiation is the MammoSite HDR Brachytherapy System (the MammoSite catheter is shown is figure 5).

The treatment is given on an outpatient basis. A flattened MammoSite balloon with catheter is inserted into the tumor resection cavity (figure 6a). Once in place, the

balloon is inflated with saline and a contrast agent (figure 6b). A CT scan is taken and a treatment plan is developed after waiting a day for edema to occur. After the balloon

Figure 5-Mammosite Balloon and Catheter

integrity and constancy is conformed treatment can begin. A radioactive seed attached to a wire delivers dose to the patient (figure 6c). After treatment the balloon is deflated and removed along with the catheter (figure 6d). The dosimetry for Mammosite HDR is based on TG-43 (Nath et al, 1995; Rivard et al, 2004), which assumes an infinite homogeneous medium. Because of heterogeneity issues, especially at the skin-air interface, there is a discrepancy in the dosimetry. This is illustrated in figure 7 where a continuous isodose curve is seen as it goes in the air region, as though is was still tissue (courtesy of Mark Rivard, Tufts University Medical Center, Boston, MA. Personal communication, 2006). This raises the possibility that the dosimetry method described herein may be applicable to breast brachytherapy as well.

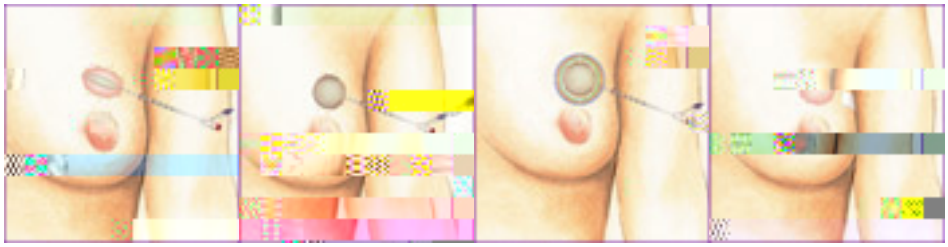

(a) (b) (c) (d)

Figure 6-(a) Flattened MammoSite Balloon with Catheter; (b) Inflated Balloon; (c) Radioactive Seed Attached to a Wire; (d) Deflated Balloon

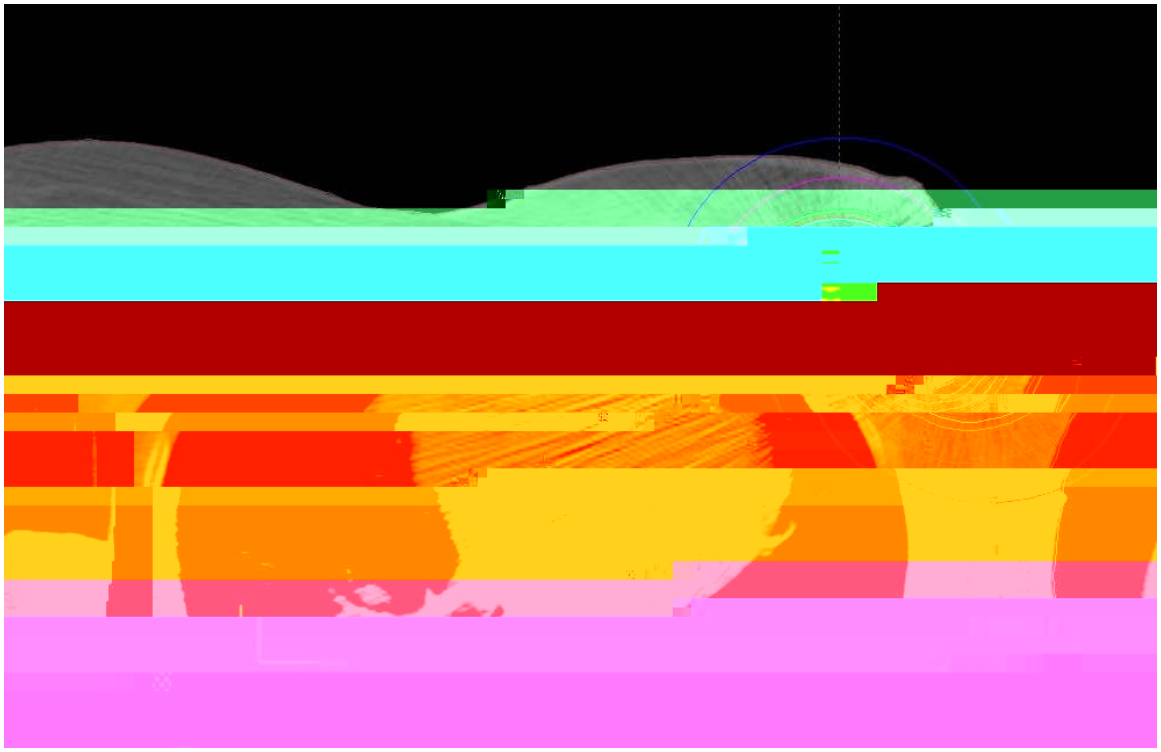

Figure 7-Isodose Contour for a Breast Implant

## 2.3 Current Brachytherapy Seed Dosimetry

In 1988 the Radiation Therapy Committee of the American Association of Physicists in Medicine (AAPM) formed Task Group No. 43 to review the publications on the dosimetry of interstitial brachytherapy sources and recommend a dosimetry protocol which would include formalism for dose calculations and a data set for the values of the dosimetry parameters for a few commonly used seed types. Since the publication of TG-

43 in 1995 (Nath et al, 1995), both the utilization of the permanent source implantation and the number of low-energy interstitial brachytherapy source models commercially available have dramatically increased. Additionally, the National Institute of Standards and Technology introduced a new primary standard of air-kerma strength, and the brachytherapy dosimetry literature grew greatly, documenting both the improved dosimetry methodologies and dosimetric characterization of particular source models. Therefore, in February of 2004 an update to TG-43 was published (Rivard et al, 2004). The update to TG-43 included: a revised defini

# CHAPTER 3

energy of 645 keV and average positron energy of 250 keV (yield of 97%). The breast seed was filled with a solution containing sodium-22. Sodium-22 has a half-life of 2.6 years, maximum positron energy of 546 keV and average positron energy of 215 keV (yield of 89.8%). In addition to positron emission, sodium-22 emits also gamma photons with an energy of 1275 keV (yield of 99.94%). Since no information on the wall thickness was available from B-D and since the manufacturer of the needle used in the

energies and their respective ranges in water and iron, the materials of interest in our experiments.

Table 1. Positron Ranges for Na-22 and F-18

| Energy (keV) | $\Lambda_{water}$ (mm) | $\Lambda_{Fe}$ (mm) |
|---|---|---|

Figure 9-Acrylic Phantom with Holes to Hold Seeds.

3.2.1 Data Extraction from the PET Images

Positron emission tomography works by detecting annihilation photons from a positron source. As discussed earlier, a positron travels a small distance, the range, and then annihilates with an electron producing two 511 keV photons that are emitted in opposite directions. The ring detector of the PET machine detects these photons using coincidence counting and registers the photons detected opposite to each other using straight lines to determine the origin of annihilation events. PET scans are used primarily for qualitative means rather than quantitative. Therefore, this is reflected in the software that reconstructs the PET image. For the purpose of this project we needed quantitative analysis. We relied on the information given in the image files (often referred to as DICOM files, because it uses this National Electrical Manufacturers Association-NEMA standard) to extract pixel intensity values. To ensure uniform brightness across many

images, the pixel intensity values of each image are automatically rescaled. The rescale values are reported in the DICOM files. IDL programming language was used to get pixel information including length, width, and thickness. The voxel dimensions were 0.585 by 0.585 by 3.27 mm. IDL was used to eliminate rescaling and to get the original pixel intensity values at and around the seed region. It was difficult to identify the values that correspond to the region of the seed for the breast case, because there were a few high false counts throughout the field of view. A commercially available program, called OSIRIS, was used to help locate the position of the seed. PET scans give a blurred extra region of space around the area of actual positron concentration. Some of the intensity that belongs in the seed region is in this blurred region. By fitting a Gaussian curve in the x, y, and z directions, the center of the seed was located, as defined by its peak centroid. By using the Gaussian curves the full width at half maximum (fwhm) in each direction was obtained. By using the fwhm the values for the standard deviation, sigma, was acquired. 3*sigma (which includes 99.75% of the Gaussian) was considered to be the maximum distance away from the center that contributes to the intensity of the seed region. It was assumed that activity detected beyond $\pm 3\sigma$ were not due to the seed activity.

3.2.2 PET Acquisition Protocols

There are various protocols in the PET software that give varying degrees of spatial resolution. Some of the parameters which affect spatial resolution included field of view (FOV), acquisition time, and reconstruction method. The parameters that were used in this project were the parameters that were best for the one seed case. Those parameters were 4-minute acquisition, 15 cm field of view, 256 by 256 resolution, and a

method of reconstruction called Ordered Subset Expectation Maximization (OSEM). Expectation Maximization is an algorithm for finding the maximum likelihood of parameters in probabilistic models where the model depends on unobserved latent variables. Expectation optimization alternates between performing an expectation (E) step, which computes an expectation of the likelihood by including the latent variables as if they were observed, and a maximization (M) step, which computes the maximum likelihood estimates of the parameters by maximizing the expected likelihood found on the E step. The parameters found on the M step are then used to begin another E step, and the process is repeated. OSEM gives better noise ratios and eliminates the streaking that is found in the Filtered Backprojection (FBP) method.

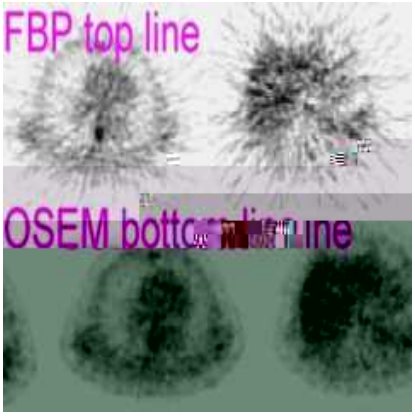


Figure 10-Streaking for FBP vs. OSEM

Filtered Backprojection uses Fourier theory to arrive at a closed form solution to the problem of finding the linear attenuation coefficient at various points in the cross section of an object. Since it is filtered backprojection the data is filtered while in the frequency domain. In the backprojection phase the bin data from the filtered sinogram is smeared back along the same lines from where the photons where emitted from. Areas

where the backprojection lines from different angles converge represents areas which contains higher concentration of radiopharmaceutical.

# CHAPTER 4

# COMPUTATIONAL

## 4.1 Computation of Dt Using MCNP Based on Measured PET Data

### 4.1.1 Data Types and Computation of Inverse Matrices

Along with the new dosimetry technique, a mathematical method was developed to link the therapeutic dose distribution to the positron annihilation event distribution (Sajo and Williams, 2004). Monte Carlo calculations and PET imaging can be used to verify this mathematical method for a few seeds, before a full computational algorithm is developed for an array of seeds. There details of the mathematical method are described in the original paper (Sajo and Williams, 2004), however the main idea can be expressed by focusing on the last steps. The dose deposited by the positrons may be written as

$$D_p(d) = \frac{1}{V_d} \int dV_s \int dV_d \; S_v(\bar{r}_s) G_p(\bar{r}_s, \bar{r}_d), \qquad (1)$$

where $V_d$ is the volume of the detector, $V_s$ is the volume of the source, $r_s$ is the position of

ing on t87 -3a -u98 0 0 7nMa[( is Tw li0000004 Tc0)68h0a[a000152h0a[a0-22.039Tf166s0a[a000152h0ara

scaled using the DICOM header information to obtain the true annihilation rate in the pixel, ε. This will be the basis for obtaining Dp.

3. Compute $D_{P,\, j \to i}$ in a matrix of pixels, i, due to each pixel-source of 0.511 photons in j, using $\varepsilon_j \left( j = 1, n \right)$ as source. This may be done using:

- MC, using CT pixel-wise HU numbers cross-meshed with the PET pixels.

rank of the matrix. When using the generalized inverse of a matrix [A(n x m)] in which the rank [R(A)] is equal to the number of columns [m] and less than the number of rows [n], then the inverse of the matrix [$A^{-1}$] is multiplied in the following order: $A^{-1}AA=A$ . When R(A) = n and <m the order of multiplication becomes $AA^{-1}A=A$. For all cases the multiplicative order that gives the best result was used.

Recently, the technology of PET imaging has proliferated. PET image reconstruction however, has problems such as partial volume effect, poor resolution, scatter contribution, system noise, and attenuation correction. To determine the effects of such problems Jarrett (Jarrett and Sajo, 2005) established the possibility and the bounds within which PET data can be used for quantitative dose assessment in support of direct prostate dosimetry. The positron dose calculated by using Monte Carlo simulation was nearly identical to the dose determined based on PET data in cases when there were no large gaps between seeds. In these cases, the error in dose compared to the calculated dose was less than 5 percent.

between the two versions verified that the discrepancy between the computed doses using a positron source versus an annihilation source is marginal.

Tally types for the Green's functions and dose were compared and the best performing tally types were selected. The MC

compared to Pinnacle computations near the phantom-air interphase. A modification was made to get a phantom suitable for the breast case. The breast case seed and phantom was imaged and the same process was done as in the prostate case. However, since there were no comparable seeds in the Pinnacle library, MCNP had to be used to compute the radial dose functions for the experimental breast seed for Ir-192 source, which in turn was used in Pinnacle.

The pixel values within the seed region including contribution from the outer region are used as the probability distribution in the source definition of the MCNP input file. Several tally types were investigated in

were the best tally types to use. The tally types investigated were f4, f5, f6, ed if8. Tally type f4 is the track length estimate of cell flux. Track length estimators are used to compute quantities of interest along free streaming trajectories. In the case of the f4 tally the quantity is flux within a cell. Tally type f5 is a next-event estimator,ted inT can be used to obtain the flux in a point detector or in a ring detector. It was the flux in the ring detector that was investigated. Since both the f4 and the f5 tally give photon flux they had to be multiplied by ICRU response functions to get the energy deposition. The units for f4 ed if5 tally are particles/cm $^2$

r the f6 tally are MeV/g. Tally type f8 is

pulse height distribution. The *f8 tally is f8 multiplied by the energy carried by the particles, thusinT is an energy deposition tally which accounts for secondary particles as well. The units for the *f8 tally are MeV. The difference between f8 ed if6 is that the former gives the dose while the latter gives the kerma. In making comparisons of the tally types the prostate case was used. Speed, relative error,ted iaccuracy where considered

while determining the best tally types. The *f8 tally was regarded as the most correct since it does not rely on a track length estimator and gives an output of energy deposition as the energy balance in the tally cell, adjusted for relativistic changes in mass. Since ideally we want to test our method using two tally types a second best tally type had to be found. Also, if the two tally types are mixed, they had to be consistent, and work well in the mathematical method together.

Relative uncertainty was given in each of the MCNP runs. A relative uncertainty of 5% or less was deemed to be acceptable and ultimately this was achieved. Relative uncertainty or statistical uncertainty refers

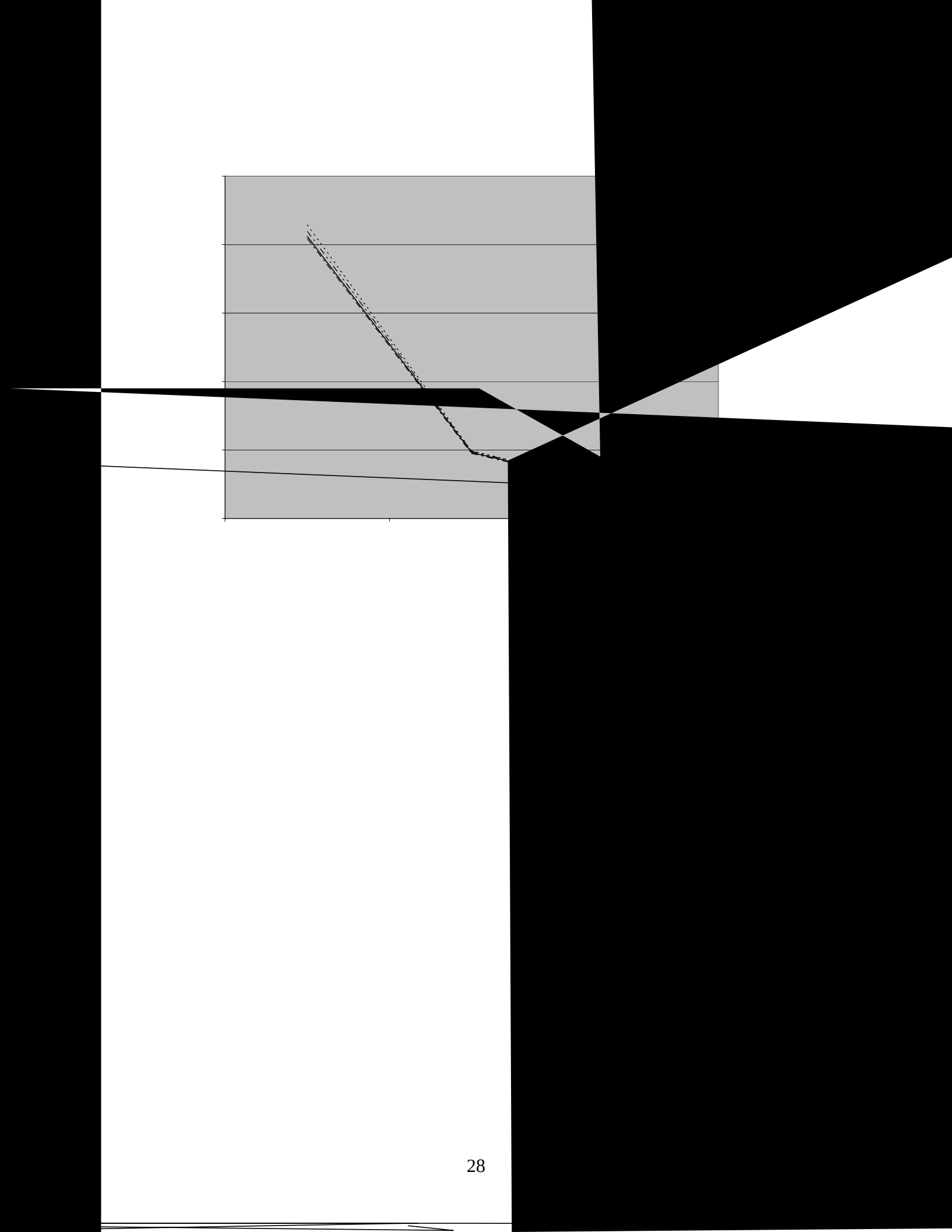

transforming the imaginary part of the matrix values of the therapeutic dose were eliminated (because their magnitude was much less than the real part) and they were compared to the expected values by using Excel. The percent difference was found by subtracting the experimental value by the expected value, dividing the result by the expected value, and multiplying by one-hundred. Also, they were compared to values acquired by Pinnacle. Since Pinnacle does not have a seed comparable to the breast case, MCNP was used to obtain the radial dose functions. An f6 tally with ring detectors was used to get the dose. The centers of the detectors were spaced 1 mm apart starting 1.5 mm from the source and ending 4.15 cm from the source. The radial dose function accounts for the effects of absorption and scatter in the medium along the transverse axis of the source. The radial dose function applies only to the transverse axis and only to points with an angle equal to $\pi/2$ with respect to the longitudinal axis of the seed. The radial dose function defines the fall off in dose rate along the transverse axis due to absorption and scatter in the medium, but can also be influenced by filtration of photons by encapsulation and source materials. The radial dose function is normalized to the dose at one centimeter from the source and it is corrected by an $r^2$ factor where r is the distance from the source. A plotting software, Surfer, was used to construct the isodose curves to visually illustrate the comparison. Also, during one of the preliminary studies the mock infinite medium data was visually compared to the half sphere data by using Surfer to plot the isodose lines. It was quantitatively compared by using Microsoft Excel to get the percent difference, which will be presented in section 5.2.

# CHAPTER 5

# RESULTS

## 5.1 Seed in Prostate

As mentioned before, nine tally cells in a 3 by 3 matrix were used for this case. In the MC computations, the tally cells were constructed as ring detectors and tallied using f6 and *f8. The output for the nine tally cells using the SW mathematical method and by using MCNP was compared. As discussed earlier, several methods of redistributing the PET intensity values were explored. These methods were mainly explored in the Ir-192 case and will be discussed in the next section. Since the different methods do not result in a better agreement, the default (100 percent of the PET counts from the region within ±3*sigma was put into the seed region) was used for the prostate case. The detectors in the midplane of the seed had a discrepancy of 12 to 15 percent. The other detectors, off midplane, had discrepancy as high as 60 percent that decreased to as low as 20 percent as the distance from the seed increased.

Since the Pinnacle software only accepts activity in units of U, which is a measure of air kerma strength, cGy $cm^2$ $hr^{-1}$, a conversion to activity units are needed when the TG-43 method is used. TG-43 gives the activity of Pd-103 in both Curie and U units. An air kerma strength of 2.6 U is equivalent to an apparent activity of 2 mCi. The comparison of the MCNP output to the pinnacle results required this type of unit conversion. The f8 tally gives output in units of MeV per tally cell and is normalized to one photon. The mass of the detectors (or tally cell) is given in grams. In some cases where the geometry is complicated, MCNP is unable to accurately determine the mass of a detector. So mass was verified by determining it manually. The detector geometry was

a rectangular torus whose volume is $2*\pi*R*s^2$ (s is the side of the square and R is the radius of the midpoint of the torus). The density of the detector was water equivalent, so the volume in $cm^3$ was equivalent the mass in grams. To simplify the calculation process one hour implant duration was calculated by Pinnacle. The conversion from MCNP output to cGy for one hour of exposure time to a radio-isotope is as follows:

$$Dose\ rate\ \frac{cGy}{hour} = \frac{number\ of\ photons}{decay} \times \frac{number\ of\ decays}{\text{second}} \times \frac{3600\,\text{sec}}{hr} \times \frac{1}{mass\ in\ grams}$$

$$\times \frac{1000\ grams}{\text{kilogram}} \times 1.602176\text{E-}13\ \frac{\text{J}}{\text{MeV}} \times \frac{1\ Gy}{\frac{J}{kg}} \times \frac{100\ cGy}{Gy} \times MCNPoutput\ \frac{MeV}{photon}\ .$$

$$Dose\ rate\ \frac{cGy}{hour} = 5.7678E-5 \times \ ^{\frac{photon\ yield}{decay}} Activity(Bq)$$

The comparison showed that the SW method appreciably underestimates the dose close to the source, but converges to the benchmark dose farther from the source. The Pinnacle software seems to slightly underestimate dose close to the source and also converges on the benchmark dose as the distance from the source increases (this however can be the result of the small difference between the dimensions of the Pinnacle and the experimental Pd-103 seed). The ratio of doses was not constant as function of distance from the source (Fig. 13), therefore the difference in dose cannot be resolved by use of a simple multiplier. This is thought to be due to the blurring in the PET image. Computations using two theoretical PET images (a single idealized voxel source and a voxel core with simulated blurring, described later in this section) showed that the effect of blurring has an important contribution to the discrepancy. The method to partition the true counts and the false counts, thus, needs to be improved.

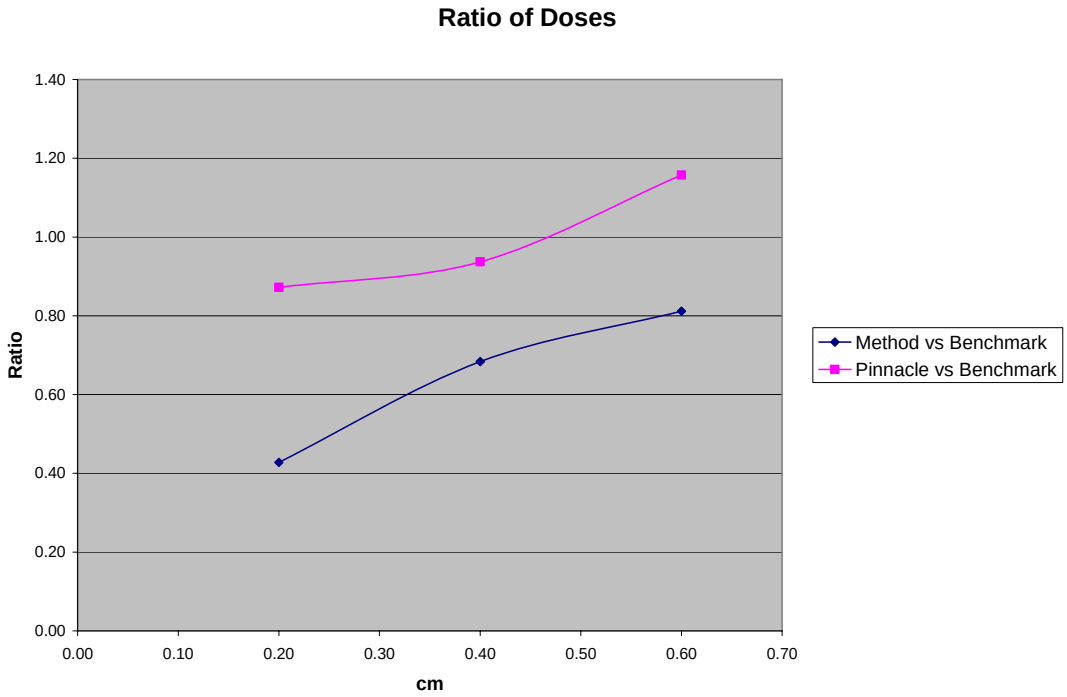


Figure 13-Ratio of Doses versus Benchmark Computation for Prostate Case

5.2 PET Intensity Redistribution to Improve Results

As mentioned earlier, several methods were explored to redistribute the PET intensity values. For the purpose of practicality using *apriori* knowledge and to get a lower discrepancy, the actual region of the seed was used to concentrate the counts.

In one method of redistributing the PET pixel intensity values, an assumption was made that a certain percentage of the values outside of the seed region are false and the complementary percentage of them are true. In general, the intensity redistribution process works by taking a portion of the values that go out to 3*sigma, summing them and multiplying the summed value by the percent that are assumed to be true counts, and adding them to the portion of the real seed to which they correspond. This process is done in the x, y, and z directions. Because the dimensions of the seed are known, and the peak centroid of the Gaussian is extracted from the image, the seed region could be determined. This is the region where the counts were added. The percentages that were evaluated as true intensity were 25, 50, 75, and 100. The difference in the resulting dose (normalized to one source photon) for these percentages was very slight. The discrepancy for the 25 and 75 percent were slightly higher than the 100 percent. The discrepancy for 50 percent was nearly identical to the discrepancy for 100 percent.

Another method of redistributing the PET pixel intensity values was to square the pixel intensity value and divide it by the sum of intensities in all pixels. This was a variable redistribution method unlike the others that just involved multiplying by a constant. The discrepancy from this method was somewhat higher, but resulted in a more continuous decrease in discrepancy over distance (Fig. 16). It is evident that the pixel intensity redistribution method is an important factor in reducing the discrepancies. No

other methods were investigated in this research, but it is recommended that future efforts be made in this area.

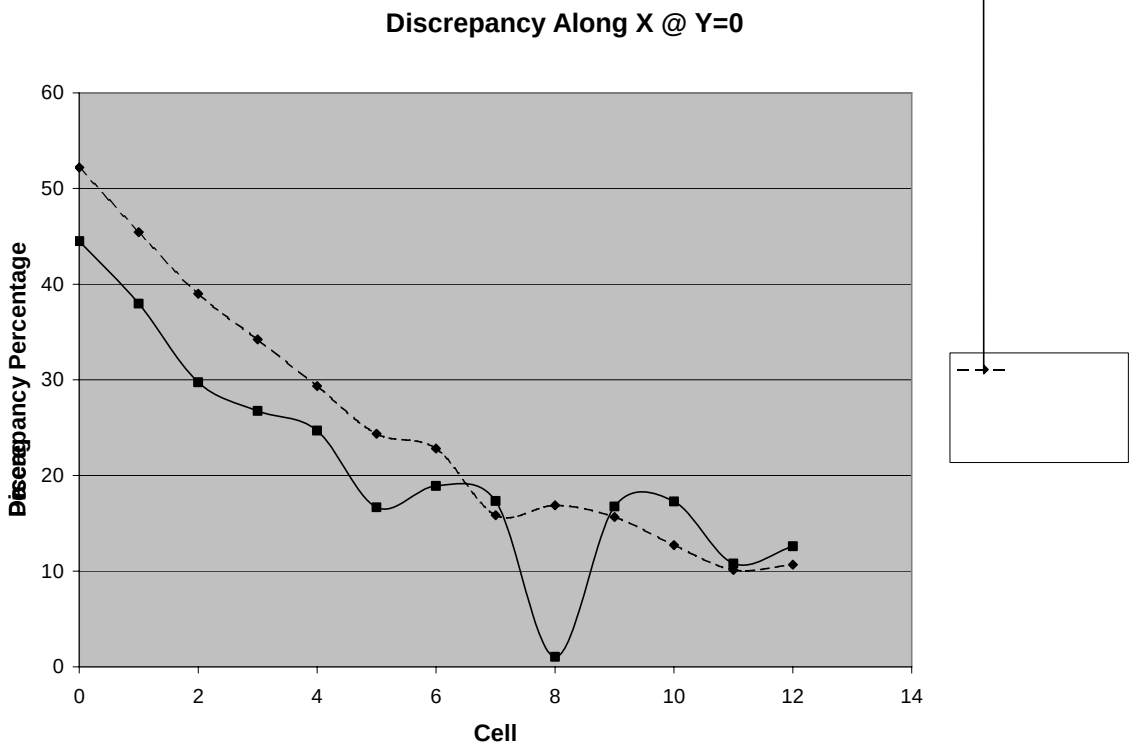

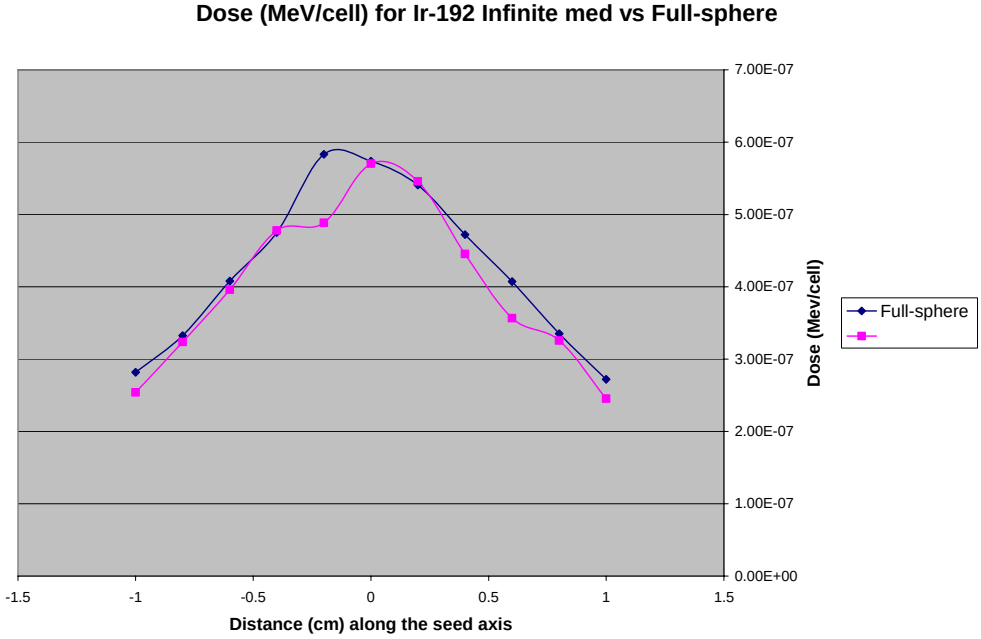
Dose (MeV/cell) for Ir-192 Infinite med vs Full-sphere
7.00E-07
6.00E-07
5.00E-07
4.00E-07
3.00E-07
2.00E-07
1.00E-07
0.00E+00
Dose (Mev/cell)
Full-sphere
-1.5
-1
-0.5
0
0.5
1
1.5
Distance (cm) along the seed axis

significantly lower than the MCNP benchmark dose close to the source. It is a possibility that for higher energy isotopes Pinnacle underestimates dose close to the source. The underprediction of the Sajo-Williams method, however, may be due to PET blurring artifacts close to the source. Nevertheless, the three dose types converge around 4 mm just as it did in the prostate case.

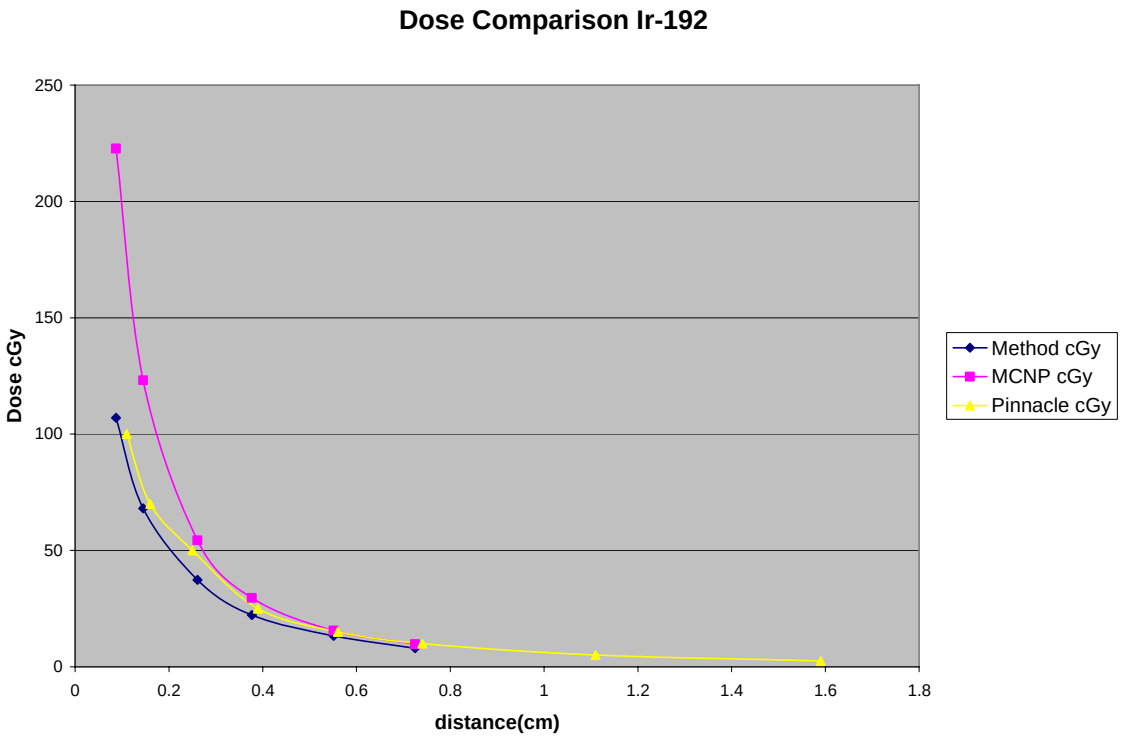


Figure 18-Dose Comparison for the Breast Case

## 5.4 Analysis of Results

Initially, it was thought that use of the f6 tally was responsible for the discrepancy close to the source. This is because f6 is a kerma tally, which is known to overpredict the dose in regions of electronic disequilibrium that may occur close to the source. This possibility was explored and it was found that the difference between the f6 and the *f8 tally was nearly negligible at distances of dosimetric interest. Nevertheless the Sajo-

Williams method was re-done for the prostate case using solely *f8 tallies and the resulting data showed that there was no significant difference from the original method (Fig. 19).

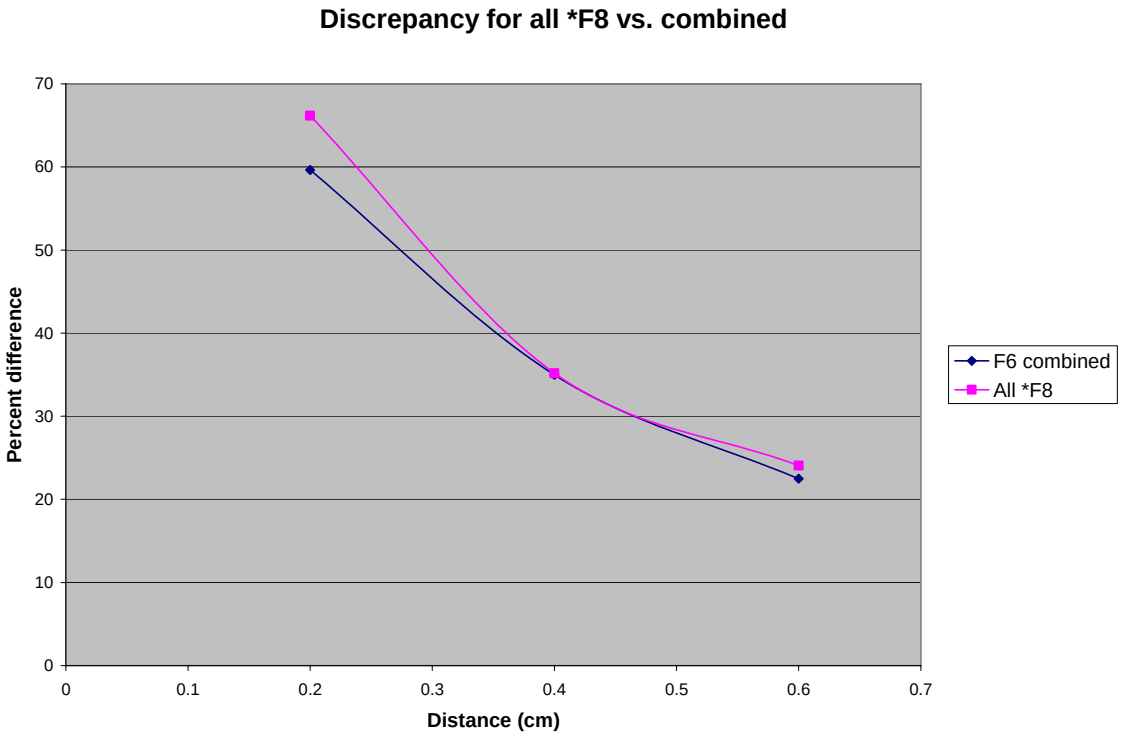


Figure 19-Discrepancy Comparison for Using only *f8 Tallies vs. Combined *f8 and f6

The effect of PET blurring:

Based on the results of the dose comparison for the prostate case the effect of blurring on the SW method was brought into question. A computational exercise was done to explore the effect of blurring on the accuracy of dose. It was found that blurring has a significant effect on the dose when computed using MC or by the SW method. For a standard seed an idealized hypothetical PET trial was compared to a hypothetical blurred PET trial and they were put through the Sajo-Williams method. Figure 20a shows the computational geometry: an idealized single voxel source of 511 keV photons is

placed in the center, and surrounded by tally voxels whose size and distribution are identical to the actual PET image voxels. Figure 20b is the same geometry, but it has a somewhat realistic blurring introduced +/- one voxel from the center voxel in all directions, surrounding the core (only 2D is shown here). The simulated PET intensity falls off as a factor of 0.6 of the nearest neighbor. This is a symmetric blurring.

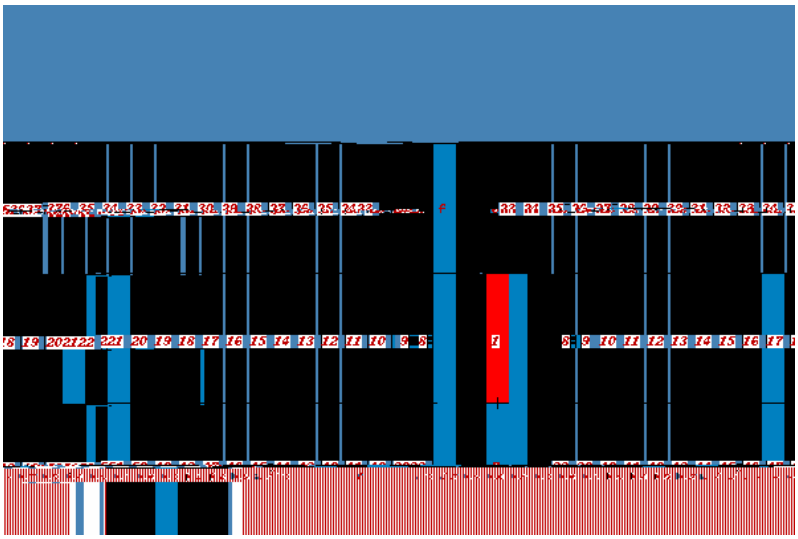

Figure 20a-Idealized Geometry with a Single Voxel Source

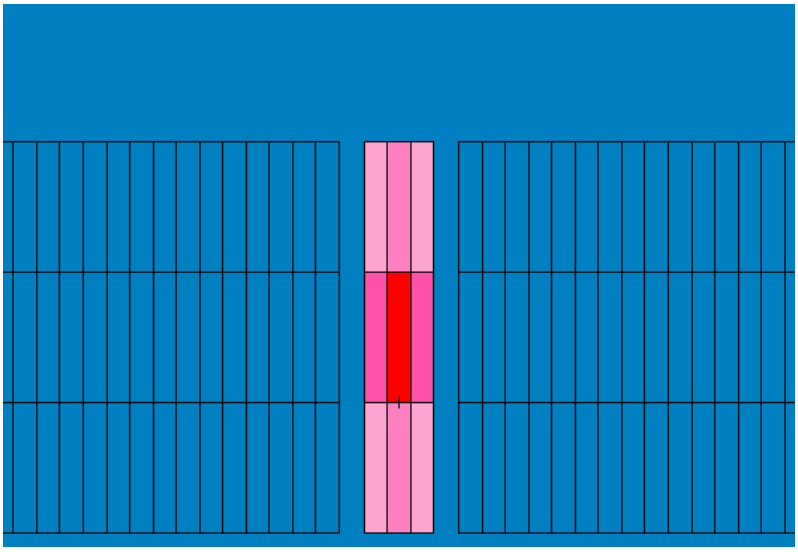

Figure 20b-Idealized Geometry with Blurred Source

As shown in Figure 21, on the midplane of the seed blurring results in an under-prediction of the dose close to the seed, by about 25%. However, off the midplane, blurring will result in an overprediction of the dose by about also 25%. This is because of two reasons; (a) the PET source is voxelized, that is the source is rectangular. If the tally cells are circular, there will be places where the corners of the voxels are close to the tally cell in the vicinity of the source. (b) More importantly, the discrepancy varies a great deal with the type of blurring introduced. Here the blurring is introduced about the center voxel within one voxel distance in all directions. Thus, this +/- 25% discrepancy at the source is a limiting condition for this kind of blurring. Hence, in practice, a method must be found that not only recaptures the PET counts but puts them in the least number of voxels.

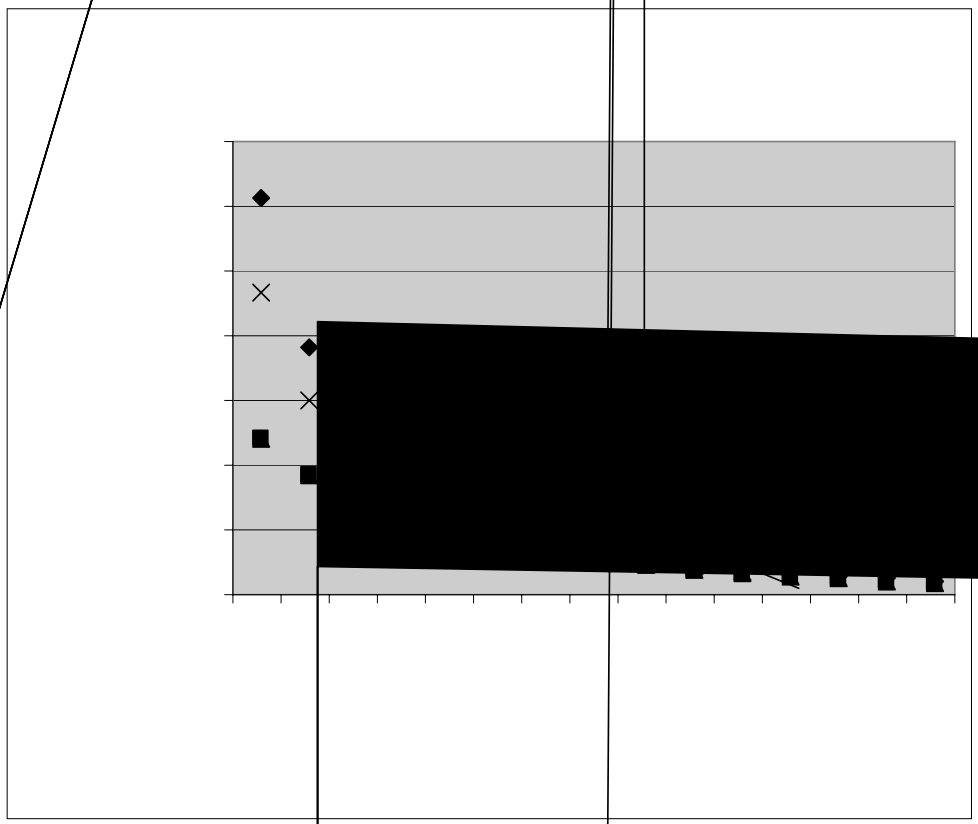

After applying the Sajo-Williams dose reconstruction method, the discrepancy for the ideal and the blurred case was even greater. Figure 22 shows the difference between

# CHAPTER 6

## SUMMARY

A new technique using direct post-implant dosimetry, which does not depend explicitly on seed orientation or position, was explored. Dose point kernels were obtained using Monte Carlo simulation for a single seed breast and prostate geometry. Green's functions were found for the positron marker and therapeutic photons. Various dose computation options in MCNP were compare and the tally types of *f8 and f6 (dose and kerma, respectively) were determined to be the best pair. A single seed was imaged for a prostate phantom and a breast phantom using a PET/CT. The pixel-wise image intensity data were extracted and used to obtain dose using MC computations for the annihilation photons for the experimental seeds. The Sajo-Williams dose reconstruction method was used to compute the therapeutic dose of the seed based on the positron marker dose. The therapeutic dose was also computed using the Pinnacle planning software. A benchmark Monte Carlo model was done to compute the therapeutic and positron doses where the precise seed geometry with source energies and distributions were known. The therapeutic dose computed using Pinnacle, computed using the Sajo-Williams method, and computed in the benchmark run was compared.

It was found that the Sajo-Williams method generally underpredicts the dose close to the source. The two main issues based on the results appear to be the discrepancy close to the source (within 4 mm) and the effect of blurring on the PET image. However, they are not independent: In a control case it was found that blurring can indeed affect dose significantly. In a series of test cases, we proved that the cause of the discrepancy in dose that is found close to the source is blurring. Although several attempts were made to

resolve this issue, one has not been found that completely solves it. However, in practice the dose very close to the source is not as important as farther away. The method of obtaining therapeutic dose investigated in this thesis can yield good results when far enough out from the source. The distance where the discrepancy from the benchmark case is reduced to within 5% is about 0.5 cm for the breast implant case and approximately 1 cm for the prostate case. A better source redefinition method that those used in this thesis is expected to further reduce the discrepancies.

Conclusions:

1. Breast case

   1a. The Sajo-Williams method has a good agreement with Pinnacle dose computations.

   1b. Both Pinnacle and the Sajo-Williams method under-predicted the dose with respect to the MC benchmark.

2. Prostate case

   2a. Pinnacle somewhat under-predicted the dose in the MCNP benchmark.

   2b. The Sajo-Williams method appreciably under-predicted the dose compared to the benchmark.

3. Possible reasons for under-prediction:

   3a. In the prostate case there were too few matrix elements, only a 3x3 dose matrix was considered, whereas the breast case, where the agreement is much better, a 21x13 dose matrix was used. This points to the possibility of numerical instability.

3b. In all cases PET image blurring imposes a limiting condition on the accuracy of the Sajo-Williams method, as shown in section 5.4.

3c. Current PET image reconstruction protocols are optimized for positron activity in the body in normal form (injected as a liquid solution). This way, the positron range is determined by the stopping power of the tissue, and significant blurring occurs. The PET image reconstruction algorithm is optimized with the presence of blurring: That is, the blurring effect is built in the reconstruction algorithm (a.k.a. kernel). Thus, it cannot take advantage of limited range blurring by a high-Z object, such as the seed wall, and possibly gives even worse results when no range blurring is present. Thus, to reduce the range blurring effects, the kernel of the reconstruction should be modified.

3d. The manufacturer regards the details about the kernel as proprietary information. In lack of access to the kernel, other methods for PET image intensity redistribution should be investigated. Deblurring methods, used in commercial photography industry, may be a viable alternative.

4.odifieodn th 0 0 3rediwe the 425ll,

# REFERENCES

Berger, MJ. ESTAR, PSTAR, and ASTAR: Computer Programs

Li Z, Fan JJ, Palta JR. Experimental measurements of dosimetric parameters on the transverse axis of a new $^{125}$I source. Medical Physics 27 (6); 1275-1280; 2000.

Moerland MA, Wijrdeman HK, Beersma R, Bakker CJG, Battermann JJ. Evaluation of permanent I-125 prostate implants using radiography and magnetic resonance imaging. Int. J. Radiat. Oncol., Biol. Phys. 7, 927–933;1997.

Nath R, Anderson LL, Luxton G, Weaver KA, Williamson JF, Meigooni AS. Dosimetry of interstitial brachytherapy sources: Recommendations of the AAPM Radiation Therapy Committee Task Group No. 43. Medical Physics 22(2); 209-234; 1995.

North American Scientific. MED3633 Pd-103 brachytherapy source. Information for physicians. April 1999.

Prestidge BR, Bice WS, Kiefer EJ, Prete JJ. Timing of computed tomography-based postimplant assessment following permanent transperineal prostate brachytherapy. Int J Radiat Oncol Biol Phys 43(5):1169-70; 1999.

Rivard MJ, Coursey BM, DeWerd LA, Hanson WF, Huq MS, Ibbott GS, Mitch MG, Nath R, Williamson JF. Update of AAPM Task Group No. 43 Report: A revised AAPM protocol for brachytherapy dose calculations. Medical Physics 31(3) 633-674, 2004.

Roberson PL, Narayana V, McShan DL, Winfield RJ, McLaughlin PW. Source placement error for permanent implant of the prostate. Medical Physics 24(2):251-257; 1997.

Roy JN, Wallner KE, Harrington PJ, Ling CC, Anderson LL. A CT-based evaluation method for permanent implants: application to prostate. Int J Radiat Oncol Biol Phys 30;26(1):163-9; 1993.

Sajo E, Williams ML. Embedded Radiation Emitter for the Localization and Dosimetry of Brachytherapy Seed Implants. US Patent 6,761,679; 2004.

Sajo E, Williams ML. Post-Implant Prostate Dosimetry without Seed Localization. Medical Physics 31(6) p. 1747, 2004.

Shultis JK, Faw RE. Radiation Shielding. American Nuclear Society, 2000.

Tubic D, Zaccarin A, Pouliot J, Beaulieu L. Automated seed detection and 3D reconstruction I: Seed Localization from Fluoroscopic Images or Radiographs.

Yegin G, D Rogers. “A Fast Monte Carlo code for Multi-seed Brachytherapy Treatments, Including Inter-Seed Effects.” Abstracts, Medical Physics 31 (6) p. 1771, 2004.

# APPENDIX A

## SAMPLE MCNP INPUT FILE

```
Pd-103dose in water from one nearest seed. Pd thickness is 23 um
c
c 1       5   -1.0     -3 4 -6
c                       inner seed cell
c
c 2       3   -7.96     -1 2 -5 #(-3 4 -6)
c                       outer seed cell
c
 3        5   -1.0     -7 #5 #6 #7 #8 #9 #10 #11 #12 #13
                       #(23 -27 28 -21 18 -20)
c                       tissue
c
 4        0             7
c                       universe outside
c
 5        5   -1.0      10 -11 -8 9
c
 6        5   -1.0      13 -14 -8 9
c
 7        5   -1.0      10 -11 -12 8
c
 8        5   -1.0      13 -14 -12 8
c
 9        5   -1.0      10 -11 -15 12
c
 10       5   -1.0      13 -14 -15 12
c
 11       5   -1.0      16 -17 -8 9
c
 12       5   -1.0      16 -17 -12 8
c
 13       5   -1.0      16 -17 -15 12
c
 14       5   -1.0      -24 23 -21 22 -25 18
c
 15     LIKE 14 BUT trcl (0.0585 0.0000 0)
c
 16     LIKE 14 BUT trcl (0.0000 -0.0585 0)
c
 17     LIKE 14 BUT trcl (0.0585 -0.0585 0)
c
 18       5   -1.0      -24 23 -21 22 -26 25
c
 19     LIKE 18 BUT trcl (0.0585 0.0000 0)
c
 20     LIKE 18 BUT trcl (0.0000 -0.0585 0)
c
 21     LIKE 18 BUT trcl (0.0585 -0.0585 0)
c
 22       5   -1.0      -24 23 -21 22 -20 26
c
 23     LIKE 22 BUT trcl (0.0585 0.0000 0)
c
 24     LIKE 22 BUT trcl (0.0000 -0.0585 0)
c
 25     LIKE 22 BUT trcl (0.0585 -0.0585 0)
c
c
```

```
c
c                  ****** end of cell definitions *******
c ======================================================================
c
c                     ****** Bounding surfaces *****

 1       pz   0.26              $top of seed
 2       pz  -0.26              $base of seed
 3       pz   0.25             $top of inner
 4       pz  -0.25             $base of inner
 5       cz   0.04             $radius outer
 6       cz   0.03             $radius inner
 7       so   1.5              $radius of universe
 8       pz   0.05
 9       pz  -0.05
 10      cz   0.15
 11      cz   0.25
 12      pz   0.15
 13      cz   0.35
 14      cz   0.45
 15      pz   0.25
 16      cz   0.55
 17      cz   0.65
 18      pz  -0.4905
 19      pz   0.0
 20      pz   0.4905
 21      py   0.0585
 22      py   0.0
 23      px  -0.0585
 24      px   0.0
 25      pz  -0.1635
 26      pz   0.1635
 27      px   0.0585
 28      py  -0.0585
c
c
c             ******* end definitions of bounding surfaces *******
c ======================================================================
c
c              ****** set other calculation parameters ******

mode     p e
c
c Importances: play Russian roulette in detectors
imp:p    4 0 4 20R
imp:e    4 0 4 20R
c ======================================================================
c
c                    ******* source definition ********
c 0.511 source.
c    Source is in encapsulation
c
  sdef  erg=0.511 par=2 cel=d1 axs=1 0 0
c
   si1 L 14
         15
         16
         17
         18
         19
         20
         21
         22
```

```
         23
         24
         25
   sp1 V  2810173.8
          2702376.9
          2203022.1
          2746429.1
          3178383.5
          2887297.1
          2327467
          2874353
          2436068.5
          2263095.3
          1853865.3
          2171014.5
c
c Note that MCNP will calculate detector response normalized to 1 source
c photon regardless to yield
c ===========================================================================
c
c                  ******* define desired tallies ********
c
  *f8:p,e  5 6 7 8 9 10 11 12 13
c
c ===========================================================================
c
c           **** define materials in problem *****
c 1: Pb
c 2: C
c 3: Stainless steel
c 4: Air (from NIST)
c 5: H2O, weight fraction from NIST) ESTEP = 8 is not needed now
c 6: Pd
c m1   82000 -1
c m2   6000 -1
m3   14000 -0.01 24000 -0.17 25000 -0.02 26000 -0.655 28000 -0.12 42000 -0.025
c m4   6000 -1.24E-4  7000 -0.7552676  8000 -0.231781  18000 -0.012827
m5   1000  -0.111894  8000  -0.888106 estep=8
c m6   46000 -1
c ===========================================================================
c           ***** Energy and cutoff cards ********
  phys:e  0.511
c  cut:e   1.0E8  0.0005
c ===========================================================================
c void
nps      4e2
prdmp 3j 1      $ retain only the last 1 dump in the mctal (bin) file
print 110 128

end of input
```

# APPENDIX B

## IDL DATA EXTRACTION PROGRAM FOR DICOM

```
pro printelement3, filename

img2=fltarr(3080192)
l=0l
values=fltarr(47)

for i=1,47 do begin
filename=strcompress(i,/remove_all)
img=read_dicom(filename)
;tvscl, img
```

```
f2=read_dicom(file2)
;f2=bytscal(f2)

for v=0,14 do begin
img4[0,v,z]=f2[s-7,t-7+v]*values[16+z]
img4[1,v,z]=f2[s-6,t-7+v]*values[16+z]
img4[2,v,z]=f2[s-5,t-7+v]*values[16+z]
img4[3,v,z]=f2[s-4,t-7+v]*values[16+z]
img4[4,v,z]=f2[s-3,t-7+v]*values[16+z]
img4[5,v,z]=f2[s-2,t-7+v]*values[16+z]
img4[6,v,z]=f2[s-1,t-7+v]*values[16+z]
img4[7,v,z]=f2[s-0,t-7+v]*values[16+z]
img4[8,v,z]=f2[s+1,t-7+v]*values[16+z]
img4[9,v,z]=f2[s+2,t-7+v]*values[16+z]
img4[10,v,z]=f2[s+3,t-7+v]*values[16+z]
img4[11,v,z]=f2[s+4,t-7+v]*values[16+z]
img4[12,v,z]=f2[s+5,t-7+v]*values[16+z]
img4[13,v,z]=f2[s+6,t-7+v]*values[16+z]
img4[14,v,z]=f2[s+7,t-7+v]*values[16+z]
endfor
endfor
;img4=bytscl(img4)
;print, img4
openu,3,'out2.txt',/append
printf,3,img4
print,img4[7,7,7]
;for w=0,46 do begin
file3=strcompress(b,/remove_all)
obj=OBJ_NEW('IDLffDICOM')
read=obj->read(file3)
obj->DumpElements, 'c:\rsi\elements.dmp'
;tv, f1
;print, *value3[0]
;value4=fltarr(47)
;value4[w]=value3[0]
;endfor
;openu,4,'out4.txt', /append
;printf,4,value3
;plot,f3
end
```

# APPENDIX C

## SAMPLE MAPLE PROGRAM FOR THE METHOD

*with*(*Spread*)

| | | | | | | | | | | | | | | | | | | | | | | | | | | | | |
|---|---|---|---|---|---|---|---|---|---|---|---|---|---|---|---|---|---|---|---|---|---|---|---|---|---|---|---|---|
| 22 | | | | | | | | | | | | | | | | | | | | | | | | | | | | |
| 23 | | | | | | | | | | | | | | | | | | | | | | | | | | | | |
| 24 | | | | | | | | | | | | | | | | | | | | | | | | | | | | |
| 25 | | | | | | | | | | | | | | | | | | | | | | | | | | | | |
| 26 | | | | | | | | | | | | | | | | | | | | | | | | | | | | |
| 27 | | | | | | | | | | | | | | | | | | | | | | | | | | | | |
| 28 | | | | | | | | | | | | | | | | | | | | | | | | | | | | |
| 29 | | | | | | | | | | | | | | | | | | | | | | | | | | | | |
| 30 | | | | | | | | | | | | | | | | | | | | | | | | | | | | |
| 31 | | | | | | | | | | | | | | | | | | | | | | | | | | | | |
| 32 | | | | | | | | | | | | | | | | | | | | | | | | | | | | |

```
gp:=GetValuesMatrix(a)
```

[*&x*, *Add*, *Adjoint*, *BackwardSubstitute*,

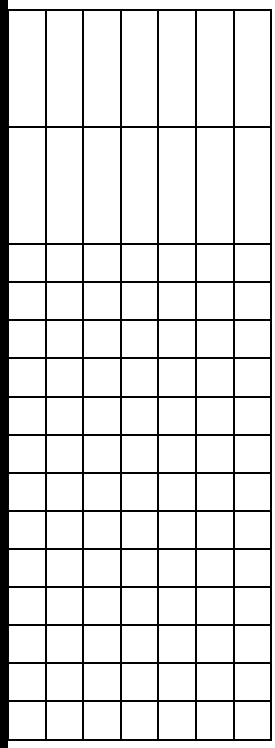

```
> Dp:=GetValuesMatrix(b2)
Warning, inserted missing semicolon at end of statement
```

$$Dp := \begin{bmatrix} 0.000323 & 0.000197 & 0.000133 \\ 0.000295 & 0.000186 & 0.000131 \\ 0.000237 & 0.000164 & 0.000122 \end{bmatrix}$$

```
>
> with(DiscreteTransforms)
```

$$[FourierTransform, InverseFourierTransform]$$

```
> gpf := FourierTransform(gp)
```

$$gpf := \begin{bmatrix} [0.00065299999999999935 + 0.\ I, \\ 0.00016350000000000017 - 0.00005167284909247152 04\ I, \\ 0.00016350000000000017 + 0.00005167284909247152 04\ I], \\ [0.00006149999999999906 - 0.00004936344801571301 04\ I, \\ 0.00004049999999999952 - 0.00003608439182435161 23\ I, \\ 0.00004849999999999930 - 0.00002800148805569684 80\ I], \\ [0.00006149999999999906 + 0.00004936344801571301 04\ I, \\ 0.00004849999999999930 + 0.00002800148805569684 80\ I, \\ 0.00004049999999999952 + 0.00003608439182435161 23\ I] \end{bmatrix}$$

```
> gtf := FourierTransform(gt)
```

$$gtf := \left[ [0.000032956666666666690 + 0.\ I,\right.$$

0.0000077216666666666756 −
0.000002901185102677868 84 I,
0.0000077216666666666756
+ 0.000002901185102677868 84 I], [
0.0000060216666666666774 −
0.000004136714678743669 33 I,
0.0000036516666666666630 −
0.000003062843178050964 14 I,
0.0000046766666666666622 −
0.000001893708882941972 22 I], [
0.0000060216666666666774
+ 0.000004136714678743669 33 I,
0.0000046766666666666622
+ 0.000001893708882941972 22 I,
0.0000036516666666666630

$$\left. + 0.000003062843178050964 14\ I] \right]$$

> $Dpf := FourierTransform(Dp)$

$$Dpf := \begin{bmatrix} [0.00059599999999999960 + 0.\ I, \\ 0.00012949999999999978 - 0.00004647669666697648528\ I, \\ 0.00012949999999999978 + 0.00004647669666697648528\ I], \\ [0.00002849999999999508 - 0.00002569208697893834 48\ I, \\ 0.00001100000000000030 - 0.00001674315780649915 28\ I, \\ 0.00001749999999999918 - 0.00000779422863405995740 \\ I], [ \\ 0.00002849999999999508 + 0.00002569208697893834 48\ I, \\ 0.00001749999999999918 \\ + 0.00000779422863405995740\ I, \\ 0.00001100000000000030 + 0.00001674315780649915 28\ I] \end{bmatrix}$$

> $gpf2 := MatrixInverse(gpf)$

$$gpf2 := \begin{bmatrix} [3915.07910881499493 + 0.\ I, \\ 40432.2731675818504 - 66139.1831420513627\ I, \\ 40432.2731675817559 + 66139.1831420514354\ I], [ \\ -1876.81627381336148 - 9123.04772310866975\ I, \\ -3.82265095253473264\ 10^{5} - 2.48512752089635382\ 10^{5}\ I, \\ 3.84737245721668588\ 10^{5} - 2.70260093820391339\ 10^{5}\ I], [ \\ -1876.81627381336876 + 9123.04772310866975\ I, \\ 3.84737245721668180\ 10^{5} + 2.70260093820391805\ 10^{5}\ I, \\ -3.82265095253473614\ 10^{5} + 2.48512752089634888\ 10^{5}\ I] \end{bmatrix}$$

> $Id2 := ((gpf.gpf2).gpf) - gpf$

$$Id2 := \begin{bmatrix} [ \\ \end{bmatrix}$$

1.08420217248550444 $10^{-19}$ − 1.56072732726740794 $10^{-18}$ I,
−2.43945488809238499 $10^{-19}$
− 9.21571846612678769 $10^{-19}$ I,
0. − 9.08019319456609964 $10^{-19}$ I], [
1.21972744404619249 $10^{-19}$ + 1.96511643762997680 $10^{-19}$ I,
−6.77626357803440272 $10^{-21}$
+ 1.82959116606928874 $10^{-19}$ I,
−3.38813178901720136 $10^{-20}$
+ 2.06676039130049284 $10^{-19}$ I], [
2.84603070277444916 $10^{-19}$ + 2.71050543121376109 $10^{-20}$ I,
1.08420217248550444 $10^{-19}$ − 9.14795583034644366 $10^{-20}$ I,
9.48676900924816380 $10^{-20}$ − 4.74338450462408190 $10^{-20}$ I]

$$\begin{bmatrix} \\ \\ \end{bmatrix}$$

> $Dtf := (gtf.gpf2).Dpf$

$$Dtf := \begin{bmatrix} \\ \\ \end{bmatrix}$$

[

0.0000302958307770961584 − 2.20228566286118088 $10^{-20}$ I,

0.0000069637273302120451 2 −

0.0000022033861355991319 7 I,

0.0000069637273302120510 6

+ 0.0000022033861355991192 6 I], [

0.0000027843315439672848 8 −

-20

$$Dt := \begin{bmatrix} [ \\ 0.000018848417823700 4020 + 1.18584612615602048\ 10^{-20}\ I, \\ 0.000010178376251210 8648 + 1.81768249650878491\ 10^{-21}\ I, \\ 0.000006837699790119 48762 - 1.23616602000184343\ 10^{-22}\ I \\ ], [ \\ 0.000015443057797868 9293 - 3.79644470527858292\ 10^{-20}\ I, \\ 0.000009173742734904 75164 - 1.80355553124419640\ 10^{-20}\ I, \\ 0.000006657509283177 27818 - 8.07889314867078206\ 10^{-21}\ I \\ ], [ \\ 0.000009931809815950 92414 - 8.62236504620068946\ 10^{-21}\ I, \\ 0.000007796361196319 02212 - 4.58710105942377446\ 10^{-21}\ I, \\ 0.000006020517638036 80869 - 2.33273542238119123\ 10^{-21}\ I \\ ] \end{bmatrix}$$

>

b5

| | | | | | |
|---|---|---|---|---|---|
| 3 | 0.00000 — 8.62\ 2 $10^{-21}$ I | 0.00000 — 4.58\ 7 $10^{-21}$ I | 0.00000 — 2.33\ 3 $10^{-21}$ I | | |
| 4 | | | | | |
| 5 | | | | | |

```
InsertMatrixIntoSelection(b5,Dt)
Warning, inserted missing semicolon at end of statement
>
```

# VITA

Jabari Robinson was born on January 13, 1981, in Baton Rouge, Louisiana. He graduated from Southern University & A&M College in 2003 with a Bachelor of Science in physics. During his time at Southern University he was involved in a publication, "Direct conversion of $TiO_2$ sol to nanocystalline anatase at $85^{o}$c", that was accepted by the *Journal of Materials Research*. In December 2006, he is expected to graduate from Louisiana State University with a Master of Science in medical physics and health physics.